PHYSICAL REVIEW B **85**, 134110 (2012)

First-principles study of electronic, vibrational, elastic, and magnetic properties of FeF_2 as a function of pressure

S. López-Moreno,[1,*] A. H. Romero,[2] J. Mejía-López,[3] A. Muñoz,[4] and Igor V. Roshchin[5,6]

[1]*Facultad de Ciencias, Universidad Nacional Autónoma de México, Apdo. Post. 70-646, México D. F. 04510, México*
[2]*CINVESTAV-Queretaro Libramiento Norponiente No 2000 Real de Juriquilla 76230 Queretaro, Qro, México*
[3]*Facultad de Física, Pontificia Universidad Católica, Av. Vicuña Mackenna 4860, Santiago, Chile*
[4]*Departamento de Física Fundamental II, Instituto de Materiales y Nanotecnología Universidad de La Laguna, La Laguna 38205, Tenerife, Spain*
[5]*Department of Physics and Astronomy, Texas A&M University, College Station, Texas 77843-4242, USA*
[6]*Materials Science and Engineering Program, Texas A&M University, College Station, Texas 77843-3003, USA*

(Received 15 December 2011; revised manuscript received 22 March 2012; published 25 April 2012)

We report systematic *ab initio* calculations of the electronic band structure, phonon dispersion relation, and the structural characterization of FeF_2 in the rutile ($P4_2/mnm$) structure as well as in several high-pressure phases by means of the generalized gradient approximation (GGA) + U approximation. Using the phonon dispersion relations, we calculated the Gibbs free energy and evaluated the phase transitions at 300 K, at which most experimental measurements are performed. Calculated Raman and infrared vibrational modes, lattice parameters, and electronic structure for all considered crystalline structures are compared with available experimental data. Our calculations show that at 5.33 GPa, the FeF_2 undergoes a second-order proper ferroelastic phase transition, rutile → $CaCl_2$-type structure. This result is supported by the softening of the elastic shear module C_s in the rutile phase, the softening (hardening) of the B_{1g} (A_g) Raman active mode in the rutile ($CaCl_2$-type) structure near the transition pressure, and the decrease of the square of the spontaneous strain e_{ss} from the $CaCl_2$-type structure. This demonstrates that the rutile → $CaCl_2$-type phase transition is driven by the coupling between the Raman active B_{1g} mode and shear modulus C_s. At 8.22 GPa, the $CaCl_2$-type structure undergoes a first-order phase transition to the $Pbca$ phase, a distorted fcc $Pa\bar{3}$ phase with a volume reduction of $\Delta V \approx 7\%$, as reported in experiments. Upon further increase of the pressure, the $Pbca$ phase transforms to a $Fmmm$ phase othorhombic center-type structure at ∼20.38 GPa, with $\Delta V \approx 2.5\%$. Finally, at 25.05 GPa, there is a phase transition to the orthorhombic cotunnite structure ($Pnma$ space group), with $\Delta V \approx 5.8\%$, which is stable up to 45 GPa, the largest considered pressure. The coordination number for the Fe ion in each phase is 6, 6, 6, 8, and 9 for rutile, $CaCl_2$-type, $Pbca$, $Fmmm$, and cotunnite structures, respectively. The evolution of the band gap, phonon frequencies, and magnetic moment of Fe ion as a function of the applied pressure is reported for all studied phases. The exchange constants J_1, J_2, and J_3, calculated for rutile and the lowest Gibbs free-energy high-pressure phases, are reported.

DOI: 10.1103/PhysRevB.85.134110 PACS number(s): 64.60.−i, 75.75.−c, 71.20.Be, 71.27.+a

I. INTRODUCTION

Rutile compounds are very important materials due to the recognized set of applications.[1–8] The most representative compound of such a structure is TiO_2, while, many other dioxides and difluorides such as VO_2, CrO_2, RuO_2, SnO_2, GeO_2 and ZnF_2, FeF_2, MgF_2, MnF_2, $CoFe_2$, $NiFe_2$ also crystallize in the rutile structure at ambient conditions. In the case of high-pressure polyforms of the rutile structure, there is a large interest in stishovite, the high-pressure polymorph of SiO_2, which appears in the lower mantle of the Earth.[9]

FeF_2 is an antiferromagnetic ionic insulator with a Néel temperature of 78.4 K.[10] Iron (II) fluoride attracted much attention due to the diversity of reported interesting properties such as the spin-phonon interaction,[11] magnon squeezing,[10] temperature dependence of the Raman active phonons,[12] exchange bias,[13] and the critical behavior of the thermal parameters at the Néel temperature[14] between others. Complete understanding of these properties requires good knowledge of structural, electronic, and vibrational properties of FeF_2, but despite all the interest, this material has been understudied.

There have been only a few studies of the crystalline structure of FeF_2 under pressure. Valerio *et al.*[15] performed theoretical studies for rutile FeF_2 up to 12 GPa. They only reported the evolution of lattice parameters and volume as a function of pressure. Ming *et al.*[16,17] reported their experimental results on the phase transition of FeF_2 under pressure by means of x-ray experiments. They found that FeF_2 undergoes a phase transition from rutile to a *distorted fluoride* structure at 8 GPa, and a subsequent phase transition to a hexagonal phase at 25 GPa. However, that publication provides the evolution of volume as a function of pressure, without any information about space group or Wyckoff positions of the high-pressure phases. Wang *et al.*[18] has considered the rutile toward $CaCl_2$-type structural phase transition, even though the Γ frequency modes show a large difference with reported experimental data. In contrast, several studies, including theoretical calculations, Raman spectroscopic, elastic, and x-ray diffraction measurements have been reported for dioxides[19–25] (SiO_2, PbO_2, IrO_2, GeO_2, and CrO_2) and other difluorides[16,17,26–30] (ZnF_2, CdF_2, CoF_2, NiF_2, and MnF_2). It was found noticed that the rutile structure in these materials undergoes a proper second-order phase transition under pressure to the orthorhombic $CaCl_2$-type structure. Hence, it is expected that FeF_2 in the rutile structure could also undergo such a phase transition.

The electronic structure of rutiles has been studied for some dioxides[31–33] and difluorides,[15,32,34–37] including FeF_2. Evolution of the energy gap as a function of pressure was

studied for ZnF_2, CdF_2, and CrO_2.[27,38] However, to the best of our knowledge, there is no information about the electronic structure or energy gap evolution with respect to pressure for FeF_2.

In regard to the vibrational properties, Porto *et al.* presented the Raman spectra for TiO_2, MgF_2, ZnF_2, MnF_2, and FeF_2.[39] More recently, Benoit and Giordano[40] reported the Raman and IR frequencies of MgF_2, ZnF_2, and FeF_2, and the phonon spectrum along the special directions $M-\Gamma-X$ and $Z-\Gamma$ at the equilibrium volume. Additionally, there are some other reports on the IR spectra of FeF_2 at that volume.[41–45] However, since there is no detailed report of the structural properties of FeF_2 under pressure, the behavior of the vibrational modes as a function of pressure is still unknown.

As a result, the dependence of thermal properties of this system on the pressure is also unknown. For example, it is expected that the B_{1g} Raman active mode softens with pressure, which could be an indication of a second-order phase transition from the rutile to a $CaCl_2$-type structure. Observations of such a transition have been reported for other difluorides.[26–30] However, the phonon dispersion relation and the behavior of phonon frequencies at high-pressure phases, the post-rutile phase for FeF_2, and many difluorides remain unknown.

The lack of information about the structural, elastic, electronic, magnetic, and vibrational properties of FeF_2 under pressure has motivated this work. In this paper, we report a density functional study of the FeF_2 in the low-energy structure (rutile) and follow the structural changes as a function of pressure, by means of generalized gradient approximation (GGA) + U for the energy exchange correlation. After considering many different candidates for high-pressure structures, we characterize only the lowest enthalpy ones by describing the changes in different physical properties as the pressure is applied. Additionally, we used the quasiharmonic approximation based on the Debye model[46] and the calculated phonon frequencies[47] to search for the minimum Gibbs free energies at a temperature of 300 K. We chose this temperature to compare our results with available experimental data. The evolution of properties for each phase was derived from the range of pressure stability obtained from the calculated Gibbs free energies.

The paper is organized as follows: In the next section, we give a detailed description of the computational procedure. The results and discussion of properties in the rutile phase at equilibrium and under pressure are in Sec. III A. In Sec. III B, we present the results for the high-pressure phases. In Sec. III C are presented the results of the magnetic properties of the studied phases. Finally, we discuss and summarize the main results of this work in Sec. IV.

II. COMPUTATIONAL DETAILS

Calculations of the total energy are performed within the framework of the density functional theory (DFT) and the projector-augmented wave[50,51] (PAW) method as implemented in the Vienna *ab initio* simulation package (VASP).[52–55] We use a plane-wave energy cutoff of 520 eV to ensure a high precision in all our calculations. The exchange-correlation energy is described within the GGA in the Perdew-Burke-Ernzerhof[56,57] (PBE) prescription. The GGA + U method is used to account for the strong correlation between the electrons in the Fe d shell, on the basis of Dudarev's method.[58] In this method, the onsite Coulomb interaction U and onsite exchange interaction J^H are treated together as $U_{\text{eff}} = U - J^H$. For our GGA + U calculations, we choose $U = 6$ eV and $J^H = 0.95$ eV for the Fe atom. The same values have been used in previous electronic-structure studies of FeF_2 with linearized augmented plane wave[36] (LAPW) and clusters of Fe_3O_4.[59] To ensure the quality of the chosen U_{eff}, we compare the electronic and structural parameters for the ground-state structure with the earlier calculations[36,37] and we find a good agreement. To further test the effect of U_{eff}, we calculate the dependence of the pressure at which the structural transition occurs for the first two phase transitions (see Fig. 7) as a function of the value of U_{eff}. As the U_{eff} changes from 3.5 to 6.5 eV, the change in the transition pressure is less than 0.4 GPa and less than 0.6 GPa for the first and the second phase transitions, respectively. This indicates that the transition is not very sensitive to the choice of U_{eff}, no matter if the transitions are of first or second order. We also found that the magnetic moment was not very sensitive to the variations of U_{eff}.

The Monkhorst-Pack scheme is employed to discretize the Brillouin-zone (BZ) integrations[60] with a mesh $4\times4\times6$, $4\times4\times6$, $4\times4\times4$, $4\times4\times4$, and $4\times8\times4$, which corresponds a set of 9, 12, 8, 8, and 16 special k points in the irreducible BZ for $P4_2/mnm$ (rutile), $Pnnm$ ($CaCl_2$-type), $Pbca$ [distorted fcc (dfcc) I], $Fmmm$ (dfcc II), and $Pnma$ (cotunnite) structures, respectively. For the additional structures considered in the high-pressure regime, we use a mesh most suitable for each case. For the electronic-structure calculations, we use the tetrahedron method with Blöchl corrections[61] with a denser mesh. In the relaxed equilibrium configuration, the forces are less than 1 meV/Å per atom in each of the Cartesian directions. The high degree of convergence for the calculated forces is required for the calculations of the dynamical matrix using the direct force constant approach (or supercell method).[62] The construction of the dynamical matrix at the Γ point is particularly simple and involves separate calculations of the forces in which a fixed displacement from the equilibrium configuration of the atoms within the unit cell is considered. The symmetry aids by reducing the number of such independent distortions to 8 independent displacements for the tetragonal rutile, 12 for the $CaCl_2$-type, $Pbca$, and $Fmmm$, and 18 for the $Pnma$ phase. Diagonalization of the dynamical matrix provides both the frequencies of the normal modes and their polarization vectors. It allows us to identify the irreducible representation and the character of the phonon modes at the zone center. The phonon dispersion curves are calculated along several high-symmetry directions in the BZ. The calculations of the phonon dispersion relation are done using the supercells $3\times3\times3$ (for rutile), $2\times3\times2$ (for $CaCl_2$-type), $2\times3\times2$ (for $Pbca$), $2\times2\times2$ (for $Fmmm$), and $2\times3\times2$ (for $Pnma$) times the conventional unit cell. This cell consists of two formula units (f.u.) for rutile and $CaCl_2$-type structure, and four f.u. for the orthorhombic phases $Pbca$, $Fmmm$, and $Pnma$. The dynamical matrices are obtained at the defined q points within the supercell and the other q points were fitted by using Fourier transform methods. The phonon dispersion curves are calculated along several

high-symmetry directions in the BZ from the minimal set of dynamical matrices. The phonon density of states (PDOS) is obtained by integration of the phonon frequencies with a very high number of k points.

III. RESULTS AND DISCUSSION

A. Rutile phase

1. Structural properties

Iron (II) fluoride (FeF_2) crystallizes in the tetragonal rutile structure with the space group $P4_2/mnm$ (D_{4h}^{14} in the Schoenflies notation) No. 136 and has two formula units per conventional cell, as seen in Fig. 1(a). Here, the iron and fluorine atoms occupy D_{2h} and C_{2v} symmetry sites. The Fe atoms are located in the Wyckoff position (WP) $2a$ (0, 0, 0) and F atoms are on $4f$ (x, x, 0). The rutile structure is characterized by the lattice parameters a and c and the x from the $4f$ WP. In the ordered state, at low temperature, the Fe^{2+}spins align alternately along the fourfold [001] z axis, showing an antiferromagnetic configuration, as indicated by the arrows in Fig. 1(a).

The Fe atoms are octahedrally coordinated by F anions that, however, do not form an ideal octahedron. The distortion depends on the structure parameters a, c/a, and x, giving rise to two different cation-anion distances. The apical distance d_a is defined between the Fe atom at $(\frac{1}{2}, \frac{1}{2}, \frac{1}{2})$ and the two anions at $(\frac{1}{2} \pm x, \frac{1}{2} \mp x, \frac{1}{2})$, while the equatorial distance d_e is referred to four anions at $(1 \pm x, 1 \pm x, 0)$ and $(1 \pm x, 1 \pm x, 1)$. Thus, the distances d_a and d_e represent the height (z axis) and the basal spacing of the *octahedron*, respectively.

In order to describe the proper magnetic behavior of the FeF_2 system, we performed collinear calculations with ferromagnetic (FM) and antiferromagnetic (AF) spin configurations. We found that the AF configuration has the lowest energy for the rutile phase. The equilibrium lattice parameters were calculated by minimizing the crystal total energy obtained for different volumes. These lattice parameters were used to fit an equation of state (EOS) with the help of a Birch-Murnaghan third-order equation.[63] The results for the equilibrium volume V_0, bulk modulus B_0, bulk modulus pressure derivative B_0', magnetic moment of Fe per f.u. μ_{Eu}, lattice parameters a and c, and WPs for rutile structure are summarized in Table I. The experimental results are taken from Refs. 48 and 49. We find a good overall agreement of our results with the previous theoretical and experimental values.[15,35,37,48,64,65] For the apical and equatorial distances d_a and d_e, we obtained the values $d_a = 2.038$ Å and $d_e = 2.145$ Å in good agreement with the experimental values $d_a = 2.03 \pm 0.07$ Å and $d_e = 2.10 \pm 0.04$ Å.[65]

2. Electronic properties

Previous theoretical results describing electronic properties obtained within the Hartree-Fock approximation[15,35] reported an overestimated band gap of ∼13 eV, as expected from that method. Those studies also discussed the role of the Jahn-Teller distortion in the electronic structure and how the spin splitting can be produced along specific crystallographic directions. Riss *et al.*[37] compared the electronic structure of rutile at the equilibrium to the structure formed with an ideal octahedron by using *ab initio* calculations with a GGA exchange-correlation functional. They reported a small energy gap of ∼0.35 eV. It is well known that GGA offers an improvement in calculating the electronic gap as compared to LSDA in strong correlated materials such as FeF_2. However, it is not sufficient to overcome the missing strong correlation. Hence, approximations such as GGA + U, meta-GGA, hybrid exchange correlations, or dynamical mean-field theory (DMFT) are necessary to account

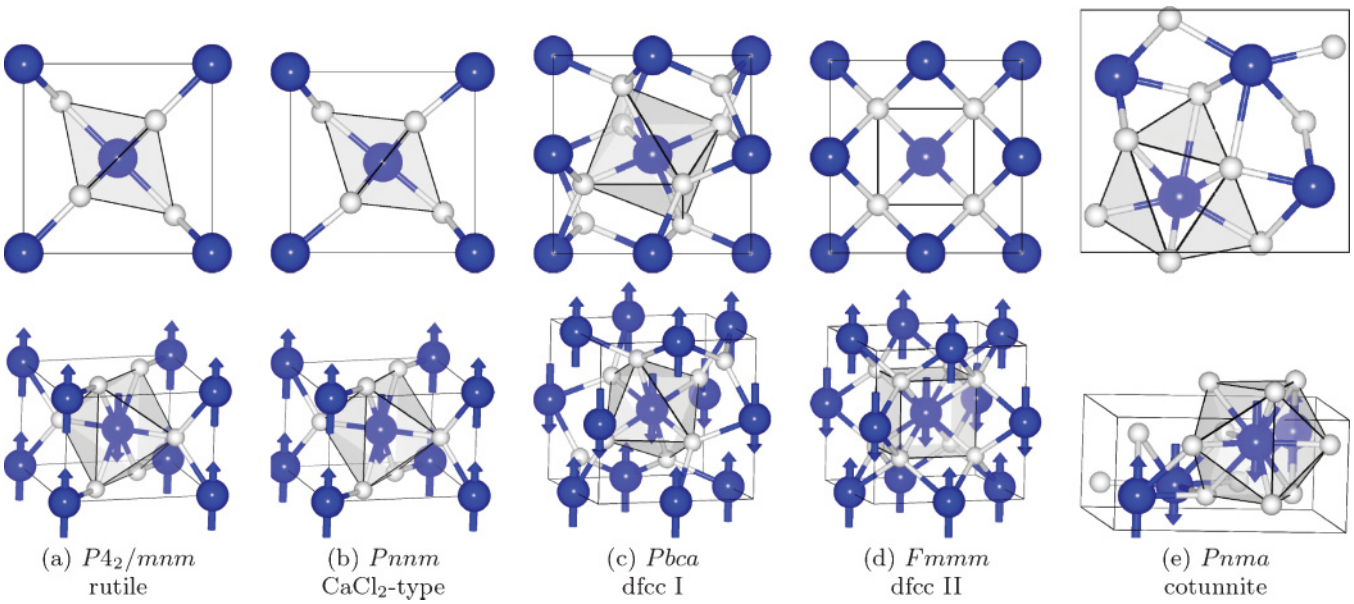

FIG. 1. (Color online) Top view and oblique projection of the crystal structure of FeF_2 in the (a) rutile ($P4_2/mnm$), (b) $CaCl_2$-type structure ($Pnnm$), (c) distorted fcc (dfcc) I ($Pbca$), (d) distorted fcc II ($Fmmm$), and (e) cotunnite ($Pnma$). Big (blue) atoms are Fe and small (white) atoms are F. Each structure shows the coordination polyhedra, the coordination number for the Fe atom for $P4_2/mnm$, $Pnnm$, $Pbca$, $Fmmm$, and $Pnma$ structures are 6, 6, 6, 8, and 9, respectively. Arrows indicate the direction of the magnetic moment of Fe atoms.

TABLE I. Structural parameters of FeF_2 for rutile and high-pressure ($CaCl_2$-type, dfcc I, dfcc II, and cotunnite) phases: a, b, and c are the lattice parameters; V_0 is the equilibrium volume; Z is the number of formula units (f.u.) in the unit cell; B_0 is the bulk modulus; B_0' is the first derivative of B_0 with respect to pressure; μ_{Fe} is the magnetic moment of Fe per f.u.; and WPs are the optimized Wyckof position for each structure.

	Rutile-$P4_2/mnm$ (0 GPa)		$CaCl_2$-type	dfcc I	dfcc II	cotunnite
	This work	Experiment[a]	$Pnnm$ (7.5 GPa)	$Pbca$ (13.2 GPa)	$Fmmm$ (22.4 GPa)	$Pnma$ (27.6 GPa)
a (Å)	4.8005	4.696	4.70347	5.0083	4.8774	5.6667
b (Å)	4.8005	4.696	4.61597	5.0432	4.8706	6.2828
c (Å)	3.3218	3.308	3.27022	5.0281	4.9461	3.0335
V_0 (Å^3)	76.55	72.96	71.0	127.0	117.5	108
Z	2	2	2	4	4	4
B_0 (GPa)	94.81	100	124.14[b]	153.92[b]	187.33[b]	206.4[b]
B_0'	4.01	4.65				
μ_{Fe} (μ_B)	3.79	3.93[c]	3.785	3.789	3.796	3.784
WPs	$2a(0, 0, 0)$		$4g(x, y, 0)$	$4a(0, 0, 0)$	$4a(0, 0, 0)$	$4c(x, \frac{1}{4}, z)$
	$4f(x, x, 0)$		$x = 0.6747$	$8c(x, y, z)$	$8f(\frac{1}{4}, \frac{1}{4}, \frac{1}{4})$	$x = 0.7716$
	$x = 0.3001$	$x = 0.3011$	$y = 0.2227$	$x = 0.3418$		$z = 0.1336$
			$2c(0, \frac{1}{2}, 0)$	$y = 0.3470$		$4c(x, \frac{1}{4}, z)$
				$z = 0.3486$		$x = 0.8478$
						$z = 0.4407$
						$4c(x, \frac{1}{4}, z)$
						$x = 0.9639$
						$z = 0.8305$

[a]Reference 48.
[b]Calculated from elastic constants.
[c]Reference 49.

for the strong correlations properly. For example, Novak *et al.*[36] using LSDA, GGA, LDA + U, and exact exchange for correlated electrons (EECE) to study the electronic structure of FeF_2 in the rutile phase, found the energy gap to be 0, 0.35, 3.0, and 4.2 eV, respectively.

In this paper, we employ GGA + U, which produces very good agreement with the most exact published results. Figure 2(a) shows the electronic band structure along the high-symmetry directions $M - \Gamma - X - R - A - Z - \Gamma$, density of states, and the Brillouin zone for the rutile phase. We obtained the energy gap of 3.14 eV, in good agreement with results obtained with LDA + U.[36] The valence band is occupied by the d orbital from Fe (mostly a hybridization between d_{z^2} and d_{xy}) and the conduction band by sp orbitals from F. According to Fig. 2(a), we predict an indirect band gap along some wave vector between $R - A - Z$ and the Γ point. Although the system is antiferromagnetic, we notice small differences between the majority and the minority spin in the occupied band, along the $M - \Gamma$ and $A - Z$. These directions correspond to the Fe-F bond, the length of which is different from the other Fe-F bond and which can distort the octahedra, an observation also noticed in Ref. 37. That work discussed how different energy levels were populated with different orbital symmetry, resulting in different energies for the spin-up and -down states. This observation leads to the conclusion that the Jahn-Teller effect is responsible for the spin splitting along specific directions.

Figure 3(a) shows the isosurface for the magnetization around the Fe atoms. This magnetization is not isotropic: the small pockets along the [110] are not present along the [100]. To investigate this magnetic anisotropy further, we calculate the Laplacian of the charge density $\nabla^2\rho_{up}$ and $\nabla^2\rho_{down}$, where ρ_{up} and ρ_{down} are the spin-up and -down electron densities, respectively. This value is plotted in Fig. 3(b), indicating where the magnetization deviates locally from the average value: enhanced (blue) or reduced (red). One can see that the magnetization is not isotropically enhanced and it is reduced along the Fe-F bonds, which means that the spin-up and -down electrons are not compensating each other along the bonds. This results in energy splitting along these directions for the up and down electrons.

3. *Vibrational properties*

It has been reported[68] that the B_{1g} Raman mode frequency decreases with decreasing temperature or increasing pressure, contrary to the typical behavior observed for other Raman active phonons. Thus, the Grüneisen parameter $\gamma_j(q)$ [$\gamma_j(q) = -\partial \ln \omega_j(q)/\partial \ln V$ for mode j, where q is the wave vector, ω is the frequency, and V is the volume] and the pressure coefficient $\partial\omega/\partial P$ are negative for this mode. This softening of the B_{1g} mode is associated with the rotation of the anions around the central Fe atom. A similar behavior has been observed in other isostructural rutile dioxides[19,24,25,69–71] and difluorides[26,30] such as SiO_2, RuO_2, CrO_2, SnO_2, GeO_2, MnF_2, and ZnF_2. Analysis of the eigenvectors corresponding to the softening of the B_{1g} Raman mode indicates a structural instability, which is the precursor for a structural phase transition.

To assess the behavior of all frequencies at the Γ point, let us analyze the dependence of all Γ modes as a function of pressure. According to group theory, the rutile structure has

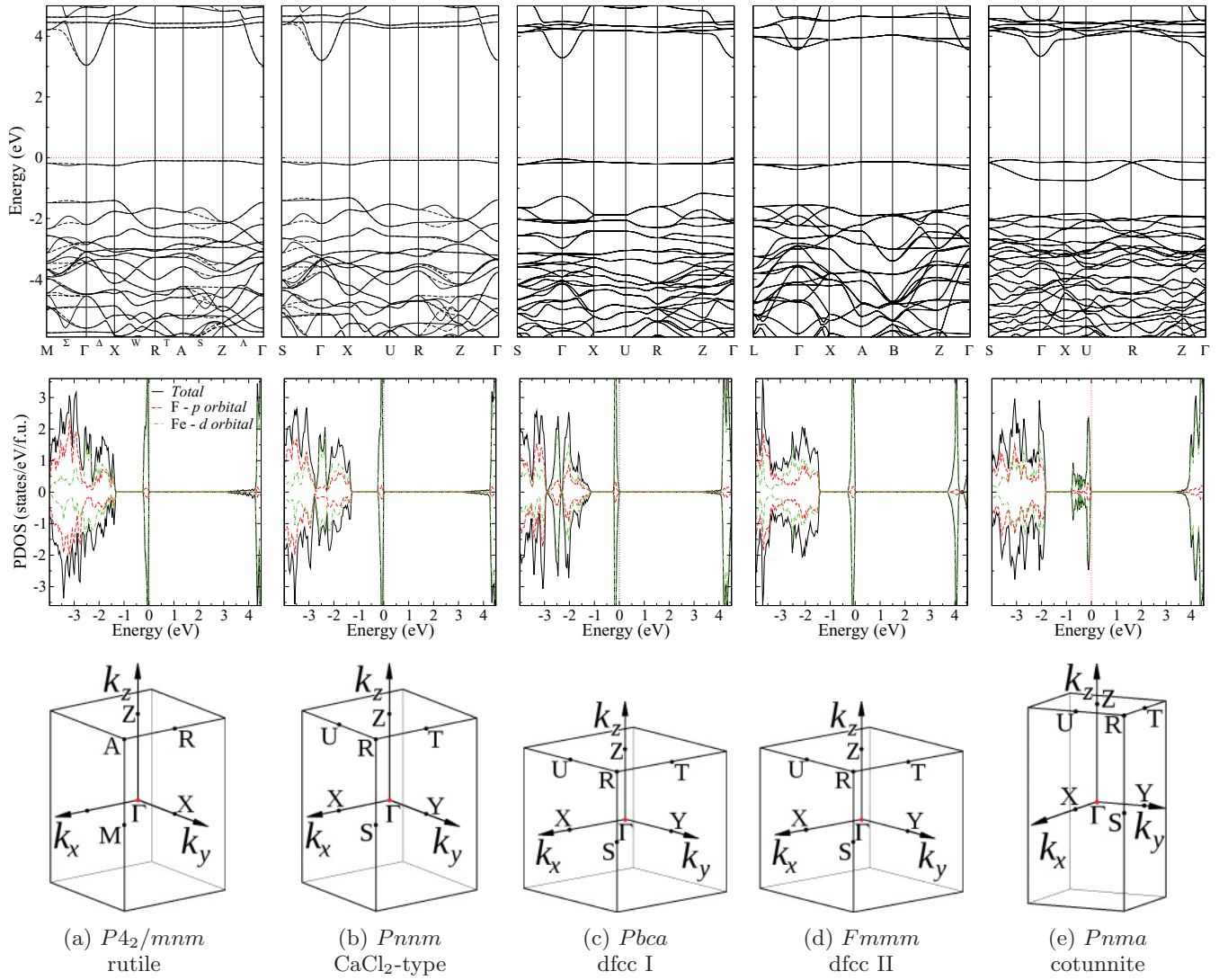

FIG. 2. (Color online) Top row: Electronic band structure along the high-symmetry reciprocal space points from the corresponding Brillouin zone (BZ); spin-up and spin-down contributions are shown as continuous and dashed lines, respectively. Middle row: Electronic density of states of FeF_2. Bottom row: The BZ for each structure: (a) rutile ($P4_2/mnm$), (b) $CaCl_2$-type ($Pnnm$), (c) distorted fcc I ($Pbca$), (d) distorted fcc II ($Fmmm$), and (e) cotunnite ($Pnma$).

the following phonon modes at the Γ point:

$$\Gamma = 2A_{2u}(\mathrm{IR}) + 4E_u(\mathrm{IR}) + B_{1g}(R) + 2B_{1u} + A_{2g} + E_g(R) + A_{1g}(R) + B_{2g}(R),$$

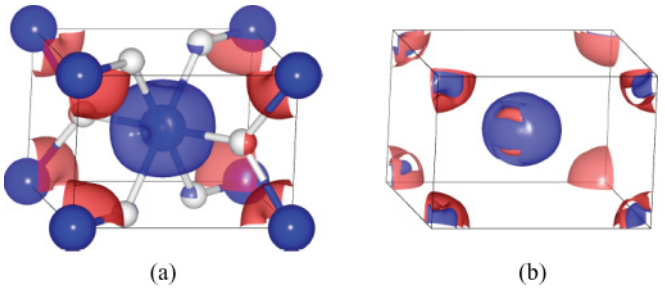

FIG. 3. (Color online) Isosurfaces of (a) the magnetization of Fe and (b) the Laplacian of the magnetization in the rutile FeF_2, red and blue are for positive and negative values, respectively.

where R and IR are for Raman and infrared, respectively. A and B modes are nondegenerate, whereas the E modes are doubly degenerate. One A_{2u} and one E_u correspond to zero-frequency acoustic modes, the rest are optical modes. The calculated phonon frequencies and the pressure coefficients for all modes for rutile phase at the Γ point are listed in Table III. As we conclude from this table, in addition to the B_{1g} Raman mode, the IR E_u and the silent modes B_{1u} and A_{2g} have negative pressure coefficients. To see the softening in the B_{1g} Raman mode more clearly, we plot the pressure dependence of the frequency of this mode in Fig. 4(a). The inset of Fig. 4(a) shows a representation of the eigenvector B_{1g} in the structure along the z axis. The F anions rotate perpendicular to the [001] direction, while Fe atoms remain fixed, resulting in an orthorhombic distortion of the tetragonal unit cell. According to Fig. 4(a), the B_{1g} Raman mode softens completely at ∼5.65 GPa. It means that rutile structure is not stable beyond this pressure. The pressure dependence of the Raman and IR

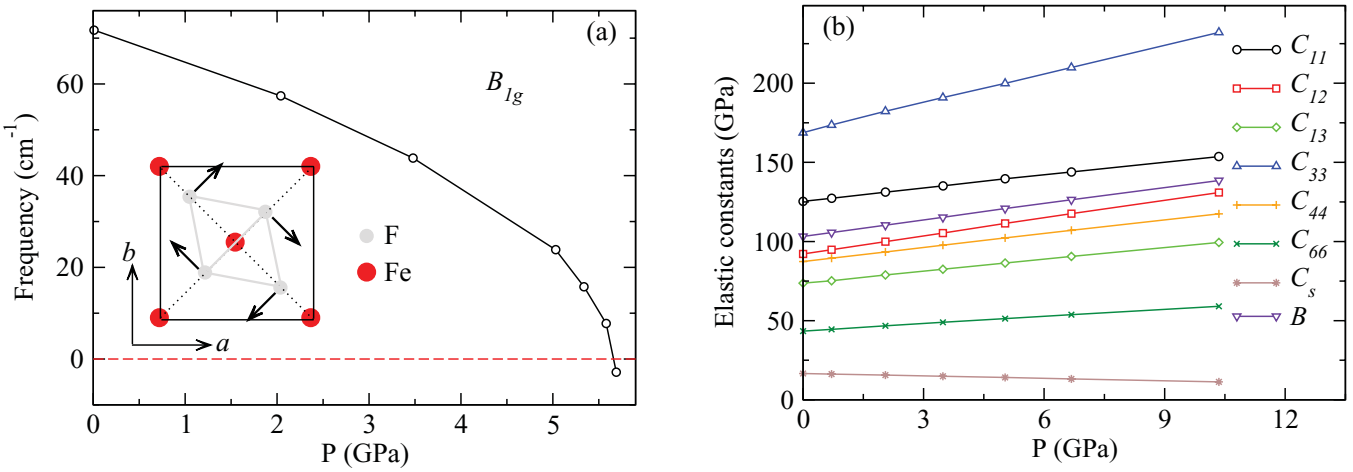

FIG. 4. (Color online) (a) Evolution of the B_{1g} Raman mode frequency ν as a function of pressure for the rutile FeF_2 until the eigenmode softens completely. The inset shows the unstable eigenvector B_{1g} mode viewed along the c axis of the rutile unit cell. Dotted lines correspond to the (110) and the $(1\bar{1}0)$ planes. The octahedron centered at $(\frac{1}{2}, \frac{1}{2}, \frac{1}{2})$ is outlined in gray. (b) Pressure evolution of the elastic constants for rutile FeF_2.

phonon frequencies at the Γ point in the rutile structure is plotted in Fig. 10.

We also calculated the full phonon spectrum of the rutile FeF_2 as a function of pressure. We found that at 2 GPa, one branch of the acoustic phonons softens in the vicinity of the Γ point, along the $\Gamma - M$ direction. As the pressure increases, this softening becomes more pronounced, so that at 5 GPa the same branch also softens in the direction $\Gamma - X$ near the Γ point. The phonon spectrum and phonon density of states are plotted in Fig. 5(a). The phonon spectrum is similar to the one reported in Ref. 40, but there are remarkable differences in the phonon density of states. In our results, the contribution from Fe and F is almost equal up to 215 cm^{-1}, while between 215 and 410 cm^{-1}, most of the PDOS comes from the F atoms. Finally, for frequencies above 410 cm^{-1}, the PDOS are almost completely dominated by the vibrations coming from the fluorine atoms.

To establish the elastic stability as a function of pressure, we also calculated the behavior of the elastic constants. The tetragonal rutile structure is characterized by six independent elastic constants C_{ij}, C_{11}, C_{12}, C_{13}, C_{33}, C_{44}, and C_{66}. The bulk modulus B can be calculated as $B = \frac{1}{3}(C_{11} + 2C_{12})$. The elastic shear modulus $C_s = \frac{1}{2}(C_{11} - C_{12})$ describes the transverse acoustic soft mode along [110] with B_{1g} symmetry. To calculate these elastic constants, we used two different methods: (1) the strain-stress relationship for rigid ions[72] implemented in VASP, and (2) the contributions for distortions with rigid ions and the contributions from the ionic relaxations.[73] The difference in the results obtained with these two methods is of the order of 5 GPa for all the elastic constants discussed above. Hence, we only list the results obtained with method 1, which are in better agreement with experimental results. We also include the experimental results at 1.5 and 298 K from Ref. 67 in Table II. Additionally, the evolution of the elastic constants with pressure is presented in Fig. 4(b). As shown in Table II and in Fig. 4(b), C_s has a negative slope ($\partial C_{ij}/\partial P$), as it has also been observed for other difluorides as MgF_2, MnF_2, FeF_2, CoF_2, NiF_2, and ZnF_2.[17,74,75] This is also related to the instability of the rutile phase at high pressures.

TABLE II. Calculated elastic stiffness constants C_{ij} of rutile FeF_2 compared to the published experimental results and their pressure derivatives $\partial C_{ij}/\partial P$. The elastic shear modulus C_s and the bulk modulus B are calculated as follows: $C_s = \frac{1}{2}(C_{11} - C_{12})$; $B = \frac{1}{3}(C_{11} + 2C_{12})$ (Ref. 66).

C_{ij}	This work (GPa)	$\partial C_{ij}/\partial P$	Expt.[a] (1.5/298 K) (GPa)
C_{11}	125.40	2.74	126.50/121.11
C_{33}	168.76	6.08	184.01/173.22
C_{44}	87.32	2.92	84.37/78.99
C_{66}	43.36	1.52	36.81/36.20
C_{12}	92.15	3.76	98.72/92.75
C_{13}	73.72	2.50	93.04/88.81
C_s	16.62	−0.51	13.89/14.18
B	103.23	3.42	109.15/103.73

[a]Reference 67.

B. High-pressure phases

The difluoride compounds with divalent cations AF_2 (A = Ca, Sr, Ba, Pb, Mg, Mn, Fe, Co, Ni, Zn, etc.), crystallize at ambient conditions in two different groups: the fluoride ($Fm\bar{3}m$) and rutile ($P4_2/mnm$) structure. At higher pressures, the AF_2 fluoride compounds such as CaF_2,[27,76] BaF_2,[77,78] and PbF_2 (Ref. 79) undergo a series of phase transitions as follows: $CaFe_2$ ($Fm\bar{3}m$) → $PbCl_2$ ($Pnma$) → Ni_2In ($P6_3/mmc$). For nonmagnetic difluoride compounds such as MgF_2 (Refs. 29 and 80) and ZnF_2,[81] the sequence for the structural phase transitions goes as Rutile ($P4_2/mnm$) → $CaCl_2$-type ($Pnnm$) → PdF_2 ($Pa\bar{3}$). While the rutile → $CaCl_2$-type phase transition is of the second order and it is properly ferroelastic,[29,81] the phase transition $CaCl_2$-type → $Pa\bar{3}$ is a first-order transition and involves a volume reduction of 6%. For these transitions, there is no change in the coordination number for the F atoms.

In the case of rutile difluorides AF_2, where A is a transition metal such as Mn, Co, and Ni, the sequence of transitions

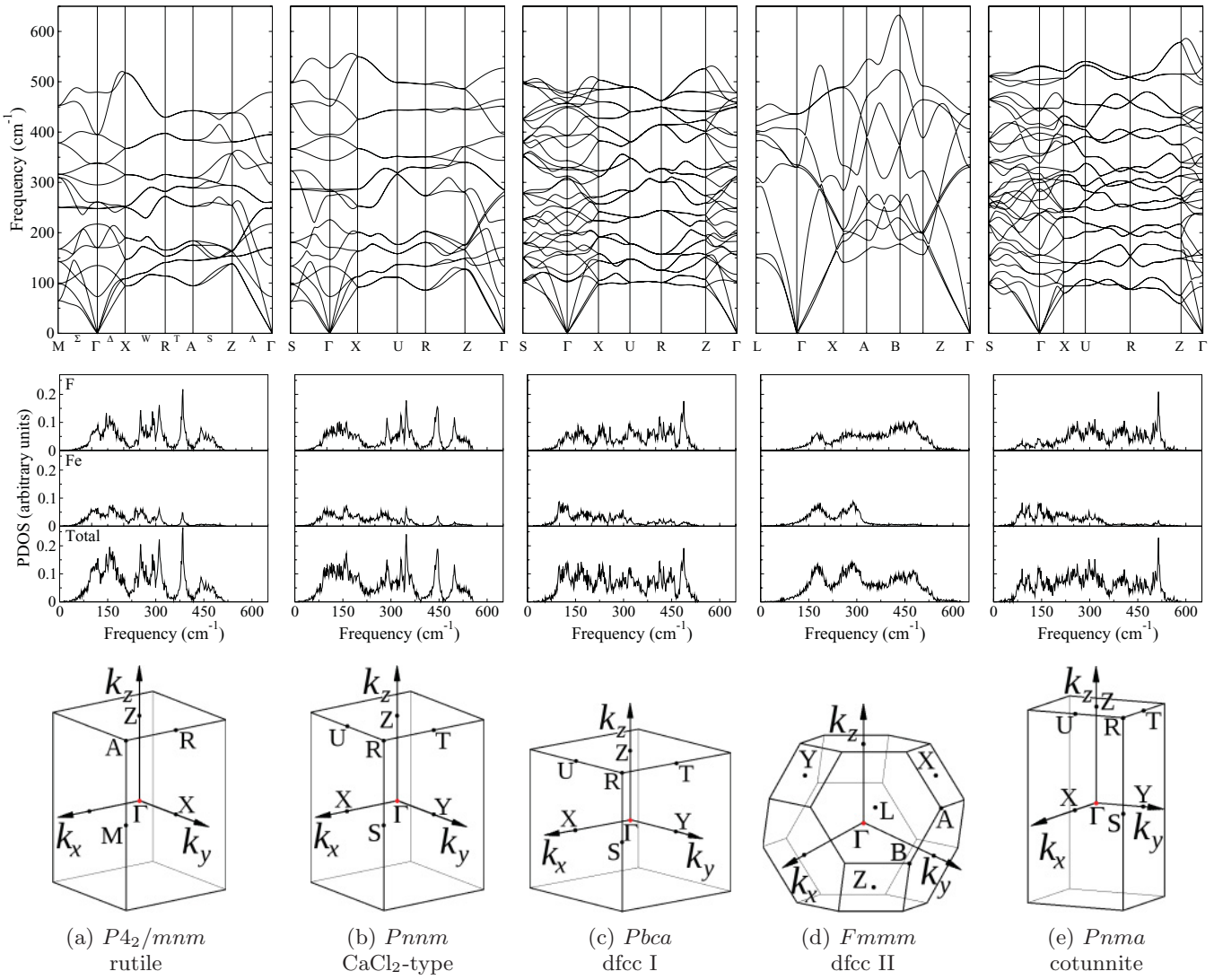

FIG. 5. Top row: Phonon dispersion relation along the high-symmetry points depicted in the Brillouin zone for each structure. Middle row: phonon density of states. Bottom row: first Brillouin zone. FeF_2 phases: (a) rutile ($P4_2/mnm$), (b) $CaCl_2$-type structure ($Pnnm$), (c) distorted fcc I ($Pbca$), (d) distorted fcc II ($Fmmm$), and (e) cotunnite ($Pnma$).

is very different. According to Ming *et al.*[17] MnF_2, CoF_2, and NiF_2 have the phase transition sequence as $P4_2/mnm$ → orthorhombic structure → DF → $PbCl_2$-type structure, $P4_2/mnm$ → DF → hexagonal structure, and $P4_2/mnm$ → orthorhombic structure → DF, respectively, where DF is "distorted fluoride" as described below. These studies were performed in the 1960s and 1970s. To the best of our knowledge, there have been no more experimental or theoretical detailed studies about the phase transitions in these compounds since then.

In the x-ray experiments performed on FeF_2, Ming and Manghnanini[16] observed that the rutile structure began to transform in a FeF_2(II) phase at about 5 GPa and completes this transformation at about 8 GPa. As the pressure increased further, a third phase, FeF_2(III), appeared and coexisted (as a metastable phase) with the phase FeF_2(II) from 25 to 32 GPa. In the high-pressure studies performed on MnF_2, CoF_2, NiF_2, and ZnF_2,[82] the phase (II) was called a *distorted fluoride*-type structure. It had a small deviation from a cubic structure ($c/a < 1.01$). The lattice parameter reported for this phase at 8.2 GPa was $a = (5.064 \pm 0.003)$ Å ($Z = 4$).[16] At the phase transition, the reduction in volume is about 8%. According to Ref. 29, the distorted fluoride structure reported in Ref. 16 corresponds to the pyrite ($Pa\bar{3}$, $Z = 4$), which is also a high-pressure phase of other dioxides and difluorides, such as IrO_2,[21] SnO_2,[23] GeO_2,[83] SiO_2,[84] and MgF_2,[29,80] ZnF_2.[81]

For FeF_2(III), Ming *et al.*[16] reported the lattice parameters $a = 3.796 \pm 0.048$ Å and $c = 4.673 \pm 0.060$ Å. Indexed as a hexagonal cell with $Z = 2$, it is similar to the hexagonal phase of $ZnBr_2$ reported in Ref. 85. At 32 GPa, Ming *et al.*[16] found a volume reduction of 5%. They suggested that the FeF_2(III) phase is probably an intermediate phase between the *distorted fluoride* and the α-$PbCl_2$-type structure. They also pointed out that due to the low number of lines in the diffraction pattern of the FeF_2(III) phase, the volume of this phase is subject to a large uncertainty (∼4%).

To study the FeF_2 phase transitions reported in the literature and to predict other possible high-pressure phases, we tested

several structures that have been previously analyzed in the study of other difluorides and dioxides. Following the results observed for the soft B_{1g} Raman mode, which is a precursor to a phase transition, we wanted to test the $CaCl_2$-type structure ($Pnnm$, $Z = 2$) to check the possibility of a second-order phase transition from rutile to this structure. Although it has not been reported in the literature, it is important to test this structure due to its appearance in many other dioxides[19–25] and difluorides[16,17,26–30] such as SiO_2, PbO_2, IrO_2, GeO_2, CrO_2, and ZnF_2, CdF_2, CoF_2, NiF_2, and MnF_2. At the same time, we include the structures of pyrite ($Pa\bar{3}$, $Z = 4$), α-PbO_2 ($Pbcn$, $Z = 4$), cubic CaF_2 ($Fm\bar{3}m$, $Z = 4$), the orthorhombic structures of $AlHo_2$ ($Pnma$, SG 62, $Z = 4$), $AlPd_2$, ($Pbca$, SG 61, $Z = 4$), and the tetragonal structure ($I4/mmm$, SG 139, $Z = 2$). To find the hexagonal phase reported in the experiments, we study many different candidates: $P622$ from SiO_2 (SG 177, $Z = 12$), $P6_222$ of $CrSi_2$ (SG 180, $Z = 3$), the Co_2P and Fe_2 ($P\bar{6}2m$, SG 189, $Z = 3$), Cu_2Te ($P6/mmm$, SG 191, $Z = 2$), the $CaIn_2$ and $InNi_2$ ($P6_3/mmc$, SG 194, $Z = 2$), HNi_2 ($P3$, SG 143, $Z = 2$), the Fe_2P ($P321$, SG 150, $Z = 3$), SiO_2 ($P3_221$, SG 154, $Z = 3$), the MoS_2 and $ZrCl_2$ ($R3m$, SG 160, $Z = 3$), V_2N ($P\bar{3}1m$, SG 162, $Z = 3$), $FeCl_2$ and $NbZr_2$ ($P\bar{3}m1$, SG 164, $Z = 2$), the $ZnBr_2$, $CaGe_2$, $CaSi_2$, and $TbFe_2$ with space group $R\bar{3}m$ (SG 166, $Z = 3$), the Ni_2Si ($P6_322$, SG 1.82, $Z = 3$), $CdBr_2$ ($P6_3mc$, SG 186, $Z = 3$). We also included the hexagonal phase of CoF_2 that resembled the high-pressure phase of SiO_2 and GeO_2 reported in Refs. 86 and 83. Its crystalline cell has the niccolite structure (NiAs, $P6_3/mmc$) with cations randomly filling one half of the octahedral sites of a hexagonally close-packed arrays of anions. To build this structure, we tested several supercells, up to $Z = 16$.

Figure 6 shows the most representative energy-volume dependences for which the relative stability and coexistence pressures of the phases can be extracted by the common-tangent construction.[87] For almost all studied phases, we tested the AF and FM spin configurations, and found that the lowest-energy configuration always corresponded to the AF state. Due to the fact that most available experimental results had been obtained at 300 K (as in Ref. 16), we also considered the effect of temperature by including corrections into the free energy. Since the calculations were done at 0 K, their outcome is the enthalpy $H = E + PV$. Hence, we needed to obtain the free energy from the vibrational contribution within the quasiharmonic approximation. Since the calculation of phonons in the entire Brillouin zone (BZ) is very expensive for all the studied phases, first, we calculated the Gibbs free energy by using the quasiharmonic Debye model reported in Ref. 46. This approach provided the first approximation for the overall behavior of the different structures as a function of temperature, at a lower computational cost. Then, we calculated only the phonons in the entire BZ for the most competitive phases to get the free energy.

Figure 7 shows the pressure dependence of the (a) enthalpy difference ΔH (0 K), and (b) Gibbs energy difference ΔG

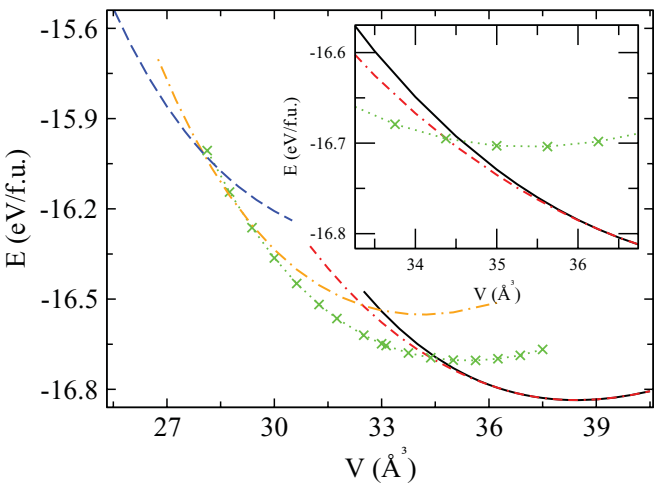

FIG. 6. (Color online) Calculated energy per f.u. as a function of volume for FeF_2. The structures shown are rutile (—), $CaCl_2$-type (– – ·), distorted fcc I $Pbca$ (· · × · ·), distorted fcc II $Fmmm$ (·—), and cotunnite $Pnma$ (––). The inset zooms in onto the area around the phase transition from rutile to $CaCl_2$-type structure.

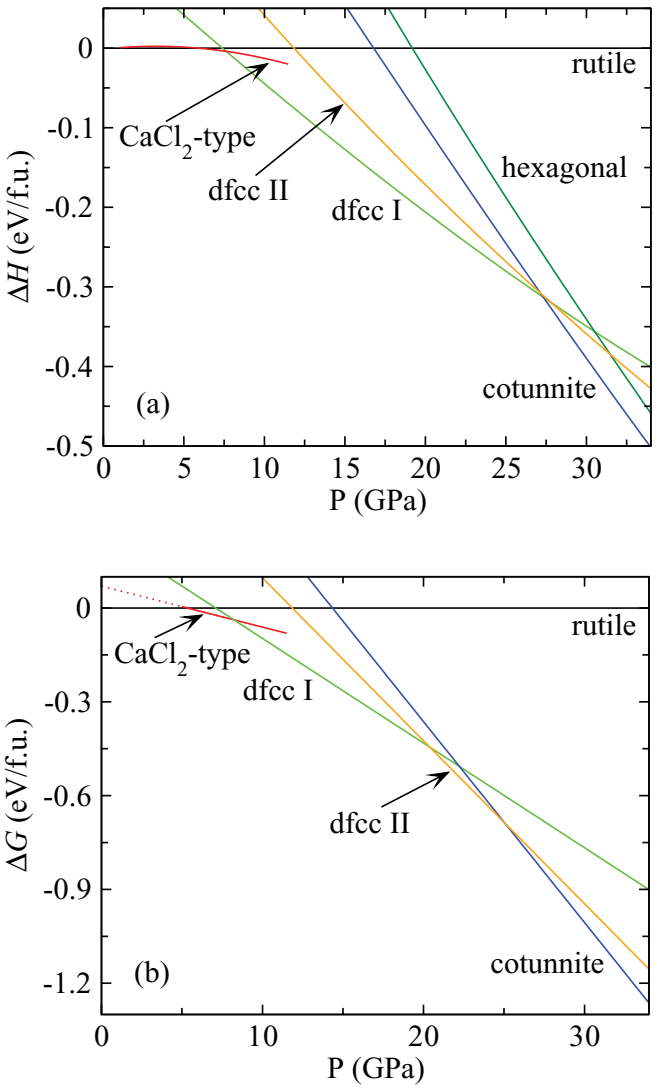

FIG. 7. (Color online) Calculated pressure dependence of (a) enthalpy difference ΔH (0 K) and (b) Gibbs energy difference ΔG (300 K), both in eV per f.u., for the most representative phases. We include the $P\bar{6}$ hexagonal phase in (a) to demonstrate that it is not competitive with any other phase.

(300 K), both in eV per f.u. The major difference between ΔH and ΔG is that the $Pnnm$ phase is stable in a slightly larger range of pressures at 300 K, and the $Fmmm$ phase becomes stable at 300 K. In Fig. 7, we plot the ΔH only for the lowest-energy hexagonal phase $P\bar{6}$ (from all the candidates considered in this work) to demonstrate that these phases are not energetically favorable compared to the other FeF_2 high-pressure phases. This finding is in contradiction with the experimental results reported in Ref. 16. We attribute this discrepancy to either the uncertainty in the x-ray diffraction analysis or to the insufficient number of hexagonal structures considered in this study.

1. *Rutile → $CaCl_2$-type structure phase transition*

According to Fig. 7(b), as the pressure increases to ∼5.33 GPa, FeF_2 undergoes a phase transition from rutile to the $CaCl_2$-type phase. In this structure, the spins are aligned as in the rutile phase [Fig. 1(b)]. For this phase, we have only two typical distances within the FeF_6 polyhedron: $d_a = 1.995$ Å and $d_e = 2.10$ Å. The space group $Pnnm$ of the $CaCl_2$-type structure is a maximal nonisomorphic subgroup of $P4_2/mnm$ (rutile). Figure 8 shows the evolution of volume V in Å^3 per f.u. One can see that there are no discontinuities in the volume between the rutile and $CaCl_2$-type structures at the transition pressure. This and the direct group-subgroup relationship indicates the possibility of a second-order proper ferroelastic phase transition.

The pressure dependence of the lattice parameters is presented in Fig. 9. At the transition pressure, the tetragonal lattice parameter a splits into unequal a and b lattice parameters of the orthorhombic $CaCl_2$-type phase, whereas the pressure evolution of the lattice parameter c remains virtually the same.

As we pointed out, the rutile → $CaCl_2$-type phase transition involves the softening of the Raman active B_{1g} mode, which corresponds to the rotation of the FeO_6 octahedra about their twofold axes parallel to the c axis of the rutile structure [see Fig. 4(a)]. Figure 1(b) shows how the polyhedron FeF_6 rotates around the c axis. According to the group theory, the orthorhombic $CaCl_2$-type phase has the following phonon mode representation at the Γ point:

$$\Gamma = 2A_g(R) + 2A_u + 2B_{1g}(R) + 2B_{1u}(\mathrm{IR}) + B_{2g}(R) + 4B_{2u}(\mathrm{IR}) + B_{3g}(R) + 4B_{3u}(\mathrm{IR}).$$

The B_{1g} Raman active mode of the rutile structure softens with increasing pressure and the Raman active mode A_g from $CaCl_2$-type structure becomes harder, as shown in Fig. 10(a). The frequencies and the pressure coefficients of the $CaCl_2$-type phase phonon modes are listed in Table III; the phonon dispersion relation and phonon density of states are plotted in Fig. 5(b). Table IV shows the relation between the phonon modes in the rutile and the $CaCl_2$-type structures. The splitting of some modes at the transition from rutile to $CaCl_2$-type phase can be seen from the correlation of the data in Table III and Figs. 10(a) and 10(b) for the Raman and IR modes. According to Fig. 5, phonon spectrum and PDOS for the rutile and $CaCl_2$-type phases are very similar. However, above 230 cm^{-1}, the PDOS for $CaCl_2$-type phase shifts up by 60 cm^{-1}. Hence, the peaks in the PDOS of the $CaCl_2$-type phase appear at higher frequencies than those for the rutile phase. Additionally, the intensities of the peaks also change. For example, the intensity of the last peak for the rutile drastically increases in the $CaCl_2$-

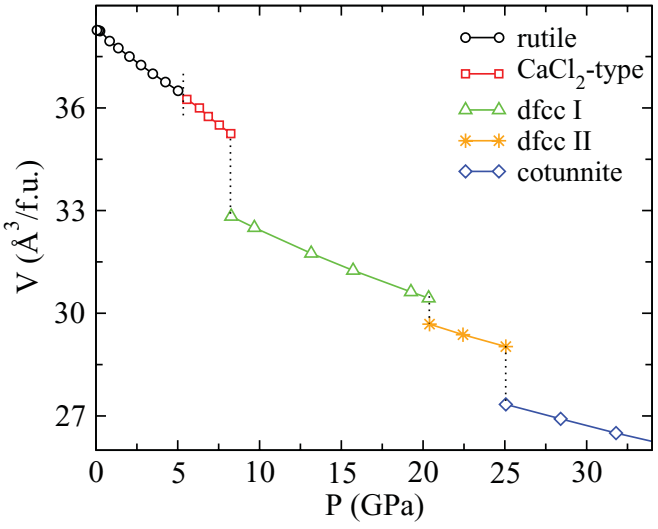

FIG. 8. (Color online) Calculated pressure dependence of the volume V in Å^3 per f.u. The volume reduction for transitions rutile → $CaCl_2$-type → dfcc I → dfcc II → cotunnite are 0%, 7%, 2.5%, and 5.8%, respectively.

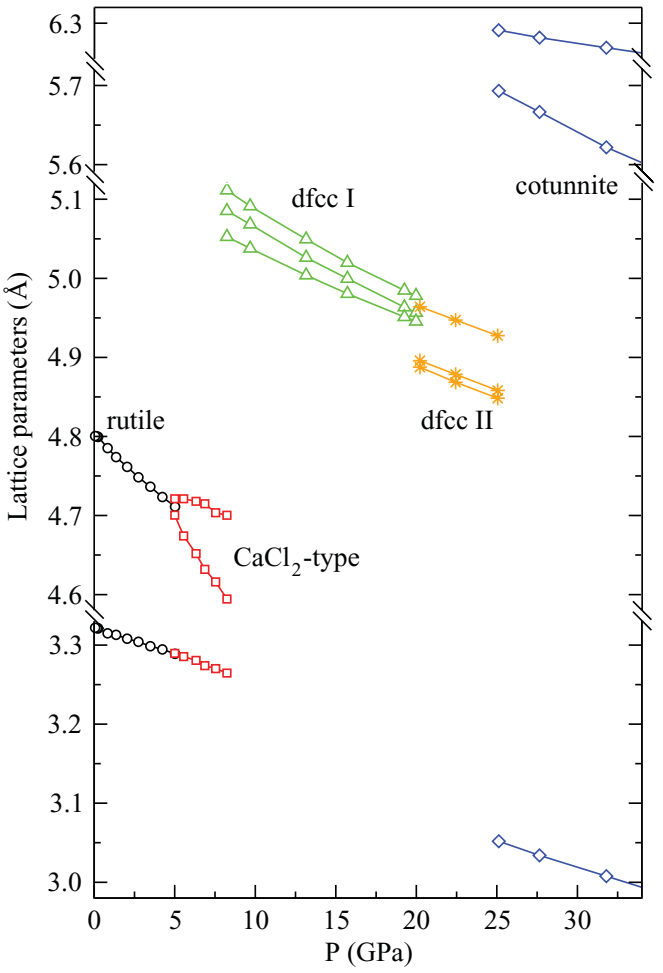

FIG. 9. (Color online) Calculated pressure dependence of lattice parameters for rutile, $CaCl_2$-type, dfcc I, dfcc II, and cotunnite phases.

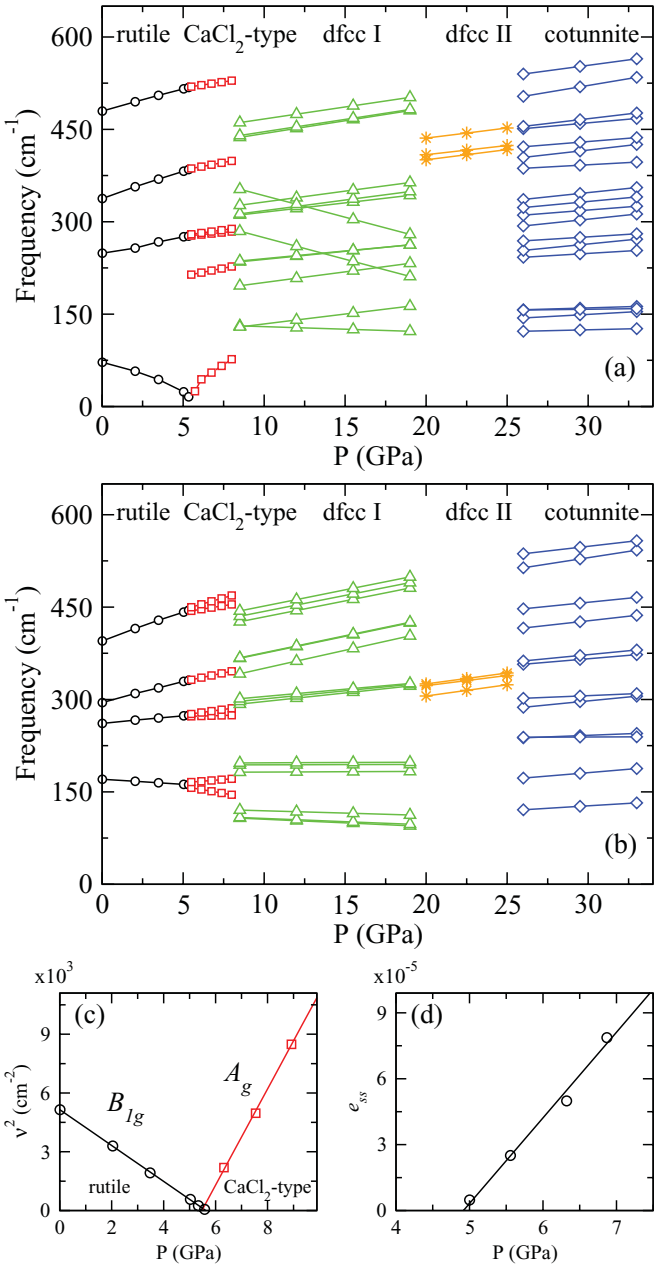

FIG. 10. (Color online) Pressure dependence of (a) Raman and (b) IR mode frequencies of all studied phases from Fig. 6, (c) the square of the Raman active B_{1g} and A_g soft modes frequencies ν^2 for rutile and $CaCl_2$-type phases, and (d) the square of the spontaneous strain e_{ss} in the $CaCl_2$-type phase of FeF_2, where $e_{ss} = (a-b)/(a+b)$.

type phase, which is the opposite to what occurs to the previous peak.

To determine the transition pressure, the evolution of the square of the B_{1g} and A_g Raman active modes frequencies ν^2 is plotted in Fig. 10(c). The transition pressure derived from the crossing point in this figure is ∼5.51 GPa, in good agreement with the value obtained from the Gibbs energy difference in Fig. 7(b). However, this transition pressure is slightly smaller than the pressure (∼5.65 GPa) at which the frequency of B_{1g} goes to zero [Fig. 4(a)]. The slopes of the squared frequencies for rutile and $CaCl_2$-type phases are $-915.8\ cm^{-2}/GPa$ and $2453\ cm^{-2}/GPa$, respectively, and the ratio of this slopes is −2.68. This ratio is slightly larger than the ideal value of 2. Nevertheless, this value is similar to the values observed for GeO_2 (−2.4) (Ref. 71) and SiO_2 (−2.27).[69] From the second-order phase transition Ginzburg-Landau theory, we can conclude that the primary order parameter is the spontaneous strain $e_{ss} = (a-b)/(a+b)$, where a and b are the lattice constants of the $CaCl_2$-type structure. Then, the order parameter should follow $e_{ss} \sim (P - P_c)^{\alpha}$, where $\alpha = \frac{1}{2}$, and P_c is the critical pressure for the rutile → $CaCl_2$-type transition. Therefore, e_{ss}^2 should be a linear function of $(P - P_c)$. We plot the pressure dependence of e_{ss}^2 in Fig. 10(d). The P_c obtained is in good agreement with the transition pressures obtained from the Raman mode softening and Gibbs energies.

All these results support the original hypothesis from Sec. III A1, where we postulated that the instability of the rutile phase at high pressures could be related with the softening of B_{1g} Raman mode and shear modulus C_s, which could be a precursor for a phase transition, as it was originally proposed in Ref . 18. Hence, the second-order phase transition from rutile to $CaCl_2$-type structure is directly related with the coupling between the Raman B_{1g} mode and the shear modulus C_s, as was observed for other difluorides.[18,80]

A very similar transition from rutile to $CaCl_2$-type structure was observed using neutron powder diffraction[28] in NiF_2, which is an antiferromagnet very similar to FeF_2. But, in the experiments performed by Ming *et al.*[16] on FeF_2, the transition discussed here was not observed. However, the same authors also reported[17] that MgF_2 undergoes a phase transition rutile → distorted fluoride at 25 GPa. Contrary to that, it was demonstrated using angle-dispersive x-ray powder diffraction and density functional theory[29] that MgF_2 has the high-pressure phase transition sequence as follows: rutile → $CaCl_2$-type → α-PbO_2 → PdF_2 (distorted fluoride) → α-$PbCl_2$. These results suggest that Ming *et al.* could not observe the rutile → $CaCl_2$-type transition in both MgF_2 and FeF_2, either due to insufficient number of data points or because the second-order phase transition was difficult to be measured due to limitations of their experimental setup.

2. *Transition to distorted fcc phases*

As pressure increases further, there is a first-order phase transition from the $CaCl_2$-type structure to the $Pbca$ phase at ∼8.22 GPa. Some difluorides and dioxides, such as IrO_2,[21] SnO_2,[23] GeO_2,[83] SiO_2,[84] MgF_2,[29,80] and ZnF_2,[81] have a high-pressure phase of a cubic structure with a space group $Pa\bar{3}$ ($Z = 4$). Our calculations indicate that this structure is unstable in FeF_2. We observe that the $Pa\bar{3}$ phase suffers distortion and transforms into the $Pbca$ structure. It is very reasonable because the $Pbca$ space group is a maximal nonisomorphic subgroup of the $Pa\bar{3}$ space group. The change in volume ΔV from $CaCl_2$-type structure to $Pbca$ at transition pressure is ∼7%. The transition pressure and ΔV is in good agreement with the experimental results for the rutile → distorted fcc transition.[16] The experimental data for the transition pressure and the ΔV are 8 GPa and 8%, respectively. In this phase, the Fe ion spins are in the opposite directions in the adjacent layers, forming the staggered magnetization

TABLE III. *Ab initio* calculated Raman, IR, and silent phonon frequencies ω (cm^{-1}), and pressure coefficients $d\omega/dP$ (cm^{-1}/GPa) of FeF_2 in the rutile, $CaCl_2$-type, distorted fcc I, distorted fcc II, and cotunnite phases at Γ point.

Rutile				$CaCl_2$-type			dfcc I			dfcc II			Cotunnite		
$P4_2/mnm$ (0 GPa)				$Pnnm$ (7.5 GPa)			$Pbca$ (13.2 GPa)			$Fmmm$ (22.4 GPa)			$Pnma$ (27.6 GPa)		
Mode	ω	ω[a]	$\frac{d\omega}{dP}$	Mode	ω	$\frac{d\omega}{dP}$	Mode	ω	$\frac{d\omega}{dP}$	Mode	ω	$\frac{d\omega}{dP}$	Mode	ω	$\frac{d\omega}{dP}$
Raman modes															
B_{1g}	71.7	73	−9.4	A_g	70.5	21.3	A_g	155.5	−0.8	B_{1g}	408.6	3.3	A_g	128.3	0.6
E_g	248.9	257	4.6	B_{1g}	225.0	5.3	B_{1g}	214.0	3.2	B_{2g}	443.8	3.3	B_{3g}	146.3	1.4
A_{1g}	337.6	340	7.8	B_{2g}	282.7	2.6	B_{3g}	248.1	3.5	B_{3g}	416.1	3.0	B_{1g}	158.4	0.8
B_{2g}	479.7	494	6.5	B_{3g}	287.1	3.5	B_{2g}	248.6	2.6				A_g	156.3	0.3
				A_g	396.5	4.9	A_g	267.3	2.5				B_{2g}	245.5	1.6
				B_{1g}	527.1	3.9	B_{2g}	325.1	−7.0				B_{1g}	258.4	2.6
							B_{3g}	329.3	3.0				A_g	271.9	1.6
							A_g	329.9	3.5				B_{2g}	298.4	2.8
							B_{1g}	343.2	3.5				A_g	340.6	2.8
							B_{1g}	456.4	−7.0				B_{2g}	313.2	2.1
							B_{2g}	458.8	4.1				B_{3g}	327.3	2.5
							B_{3g}	479.6	3.9				B_{2g}	389.0	1.4
													B_{3g}	409.5	3.0
													B_{2g}	425.5	2.1
													A_g	454.3	2.4
													B_{1g}	459.9	3.1
													A_g	511.5	4.4
													B_{2g}	546.1	3.5
Infrared modes															
E_u	170.4	175/230	−1.7	B_{3u}	146.8	−4.5	B_{1u}	102.1	−1.2	B_{1u}	314.5	3.6	B_{1u}	123.9	1.6
E_u	261.1	245/249	2.5	B_{2u}	171.1	2.1	B_{3u}	103.9	−1.1	B_{3u}	333.8	3.5	B_{3u}	176.5	2.2
A_{2u}	294.9	312/387	6.8	B_{2u}	273.8	0.7	B_{2u}	117.1	−0.7	B_{2u}	330.4	3.3	B_{1u}	239.5	1.0
E_u	395.0	408/527	9.3	B_{3u}	284.4	3.7	B_{2u}	182.7	0.1				B_{3u}	238.6	0.1
				B_{1u}	343.7	5.5	B_{3u}	194.4	0.1				B_{2u}	291.7	2.6
				B_{3u}	451.7	4.2	B_{1u}	197.6	0.1				B_{1u}	303.5	1.1
				B_{2u}	465.5	7.6	B_{3u}	305.6	2.8				B_{3u}	361.2	2.2
							B_{1u}	309.3	2.6				B_{2u}	366.9	2.6
							B_{2u}	312.6	2.3				B_{3u}	421.1	2.9
							B_{2u}	369.5	5.9				B_{1u}	451.6	2.6
							B_{1u}	392.8	5.5				B_{1u}	521.1	4.1
							B_{3u}	393.7	5.5				B_{3u}	541.8	3.0
							B_{3u}	450.7	5.2						
							B_{1u}	459.6	5.2						
							B_{2u}	468.5	5.3						
Silent modes															
B_{1u}	134.7		−0.47	A_u	132.9		A_u	157.2					A_u	98.3	
B_{1u}	338.7		6.60	A_u	391.6		A_u	162.9					A_u	314.4	
A_{2g}	234.9		−1.76				A_u	199.9					A_u	345.4	

[a]References 39 and 40 for Raman and IR frequencies, respectively.

[Fig. 1(c)]. At 13.2 GPa, the FeF_6 octahedron is more distorted than in the rutile or $CaCl_2$ type. The corresponding three pairs of distances in the irregular octahedron are $d_1 = 2.026$ Å, $d_2 = 2.066$ Å, and $d_3 = 2.073$ Å.

According to the group theory, the orthorhombic $Pbca$ phase has the following Γ phonon modes:

$$\Gamma = 3A_g(R) + 6A_u + 3B_{1g}(R) + 6B_{1u}(\mathrm{IR}) + 3B_{2g}(R) + 6B_{2u}(\mathrm{IR}) + 3B_{3g}(R) + 6B_{3u}(\mathrm{IR}).$$

As presented in Table III, the Raman active modes A_g, B_{2g}, and B_{1g} have negative pressure coefficients with values of −0.8 cm^{-1}/GPa, −7.0 cm^{-1}/GPa, and −7.0 cm^{-1}/GPa, respectively. It is noteworthy that the latter value is very close to the value for B_{1g} in the rutile phase. On another hand, the IR B_{1u}, B_{3u}, and B_{2u} modes also have negative pressure coefficients of −1.2 cm^{-1}/GPa, −1.1 cm^{-1}/GPa, and −0.7 cm^{-1}/GPa. For this phase, the phonon spectrum and PDOS show features that are different compared to the rutile and $CaCl_2$-type phases. In the dfcc I phase, the main contribution due to Fe ions is below 300 cm^{-1}, and for higher frequencies almost all PDOS is due to F atoms. At the end of the PDOS, we see a sharp peak around 490 cm^{-1}, which also

TABLE IV. Phonon mode correlations between the rutile and the $CaCl_2$-type phases.

Rutile	$\Longleftrightarrow$	$CaCl_2$-type	Rutile	$\Longleftrightarrow$	$CaCl_2$-type
A_{1g}	$\Longleftrightarrow$	A_g	A_{2u}	$\Longleftrightarrow$	B_{1u}
B_{1g}	$\Longleftrightarrow$	A_g	$3E_u$	$\Longleftrightarrow$	$3B_{2u} + 3B_{3u}$
B_{2g}	$\Longleftrightarrow$	B_{1g}	A_{2u}	$\Longleftrightarrow$	B_{1u}
E_g	$\Longleftrightarrow$	$B_{2g} + B_{3g}$	E_u	$\Longleftrightarrow$	$B_{2u} + B_{3u}$
A_{2g}	$\Longleftrightarrow$	B_{1g}	$2B_{1u}$	$\Longleftrightarrow$	$2A_u$

appears in the $CaCl_2$-type phase. Overall, the PDOS in dfcc I phase is less sharp than in the rutile or $CaCl_2$-type phases. This is mainly due to an increase of the number of phonon branches and larger dispersion. For this and the other orthorhombic phases, we follow (with an exception of the dfcc II) the same path along the Brillouin zone used for the rutile phase. According to Fig. 5, the acoustic branches for dfcc I have larger dispersion than in the rutile and $CaCl_2$-type phonon spectra.

At ∼20.38 GPa, there is a phase transition from dfcc I to the *Fmmm*-type structure. We did not find any dioxide or difluoride corresponding to this structure in the Inorganic Crystal Structure Database (ICSD). To find this structure, we used the CaF_2-type (SG $Fm\bar{3}m$) as the input crystal structure. It is unstable in the FeF_2 compound: after distortion, it transforms to the *Fmmm* structure, so we call it dfcc II. The dfcc II structure is stable in the interval of pressures that is barely 4.7 GPa (see Figs. 7 and 8). This phase is a face-centered orthorhombic structure, with a symmetry closer to the $Pa\bar{3}$ than to the dfcc I [see Fig. 1(d) and Table I]. For this phase, we also calculated the phonon spectrum, phonon density of states, and pressure evolution of the phonon frequencies and reported them in Table III and Figs. 5(d), 10(a), and 10(b). As shown in Fig. 5(d), we used the primitive Brillouin zone, $Z = 1$, to choose the high-symmetry special points to build the phonon spectrum. This differs from the band-structure calculations where we used the cell with $Z = 4$, due to the fact that FeF_2 is an antiferromagnetic compound and therefore it is not stable in a primitive cell. Since dfcc I and dfcc II phases are the structures derived (distorted) from the fcc, the evolution of the cell parameters is very similar, so none of the axes is more compressible than the others. In the dfcc II, the Fe coordination number is eight, all $d_{\text{Fe-F}}$ distances are equal to 2.12 Å, and the angles $\theta_{\text{F-Fe-F}}$ in the FeF_8 polyhedron are between 69.7° and 70.9°. In this phase, the FeF_8 coordination polyhedron has all angles equal to 90° and the cell parameter of 2.44 ± 0.04 Å, which is almost a perfect cube with the polyhedral symbol *CU-8*, according to IUPAC.[88] In this phase, the spins are aligned as in the dfcc I phase [see Figs. 1(c) and 1(d)].

According to the group theory, the orthorhombic *Fmmm* phase has the following phonon modes at the Γ point:

$$\Gamma = B_{1g}(R) + 2B_{1u}(IR) + B_{2g}(R) + 2B_{2u}(\text{IR}) + B_{3g}(R) + 2B_{3u}(\text{IR}).$$

As we can see from this equation and Table III, there are three Raman, three IR optical modes, and three acoustic modes (B_{1u}, B_{2u}, and B_{3u}). We found that the phonon dispersion relation for dfcc I and dfcc II are stable only in the pressure range shown in the Gibbs energy difference plot in Fig. 7(b).

3. Cotunnite phase

At ∼25.05 GPa, FeF_2 undergoes the last phase transition from dfcc II to the *Pnma* structure. This phase is the same as that of the mineral cotunnite. The cotunnite structure has also been observed as a high-pressure phase in other compounds such as PbF_2,[79] MgF_2,[29] MnF_2,[5] SnO_2,[89] TiO_2,[90,91] and GeO_2.[92] The cell constants ratios (at 27.6 GPa) $a/b = 0.902$ and $(a + b)/c = 3.939$ are in the limit of the cotunnite-type structures, for which a/b ranges from 0.80 to 0.90 and $(a + b)/c$ from 3.3 to 4.0 (see Ref. 29 and references therein). In this phase, the coordination number for the Fe atoms is 9, and the distances $d_{\text{Fe-F}}$ in the polyhedral FeF_9 are 1.977, 2.194, and 2.443 Å, and three pairs of 2.056, 2.144, and 2.369 Å. The shape of this polyhedron is similar to the tricapped trigonal prism with the symbol *TPRS-9*, according to IUPAC.[88] Figure 9 shows that the *a* axis is more compressible than the other cell parameters. This is mainly due to the fact that along the *a* direction, one bond length in the FeF_9 polyhedron is larger than the other eight. We found that the cotunnite phase was stable at least up to ∼45 GPa, which was the largest pressure considered in this work.

According to the group theory, the orthorhombic *Pnma* phase has the following Γ phonon modes:

$$\Gamma = 6A_g(R) + 3A_u + 3B_{1g}(R) + 6B_{1u}(\text{IR}) + 6B_{2g}(R) + 3B_{2u}(\text{IR}) + 3B_{3g}(R) + 6B_{3u}(\text{IR}).$$

The phonon spectrum of this phase is more similar to the spectrum of the dfcc I phase than to that of the others. Similarly to the dfcc I and dfcc II phases, for the cotunnite phase, the main contribution to the PDOS for frequencies above 375 cm^{-1} is due to the F ions. We calculated the phonon spectrum in the range from 20.5 to 32 GPa and found that no phonon is softened within this pressure range.

The value of the bulk modulus B_0 for the rutile phase is in very good agreement with both the experimental data[48] and the value obtained by means of elastic constants.[67] At high pressures, the value of *B* increases from one phase to another, rutile (94.81 GPa at 0 GPa) → $CaCl_2$-type (124.14 GPa at 7.5 GPa) → dfcc I (153.92 GPa at 13.2 GPa) → dfcc II (187.33 GPa at 22.4 GPa) → cotunnite (206.4 GPa at 27.6 GPa). For comparison, the bulk modulus of the TiO_2 cotunnite phase was experimentally measured and calculated to be 431 GPa (Ref. 93) and 380 GPa,[90] respectively. It is clear that the cotunnite phase is more compressible in FeF_2 than in TiO_2.

Figure 11(b) shows the pressure dependence of the Fe magnetic moment μ_{Fe} in μ_B/f.u for the structures presented in Fig. 6. There is no significant change in μ_{Fe} at the transition pressure from the rutile to $CaCl_2$-type phase. The evolution of the magnetic moment with pressure for each phase in Fig. 11(b) can be fitted with the equation $\mu_{\text{Fe}} = a + bP$, where *b* is the slope in μ_B/GPa and *P* is the pressure. The values of *b* for rutile, $CaCl_2$-type, dfcc I, dfcc II, and cotunnite are 0.94, 0.74, 0.62, 0.47, and 0.44 mμ_B/GPa, respectively. The changes in the magnetic moment are small within all equilibrium pressure ranges for each phase. Similar trends are observed for the electronic gap, where the constant *b* for rutile, $CaCl_2$-type, dfcc I, dfcc II, and cotunnite are 18.3, 19.4, 17.9, 18.2, and 11.8 meV/GPa, respectively. These values are rather small,

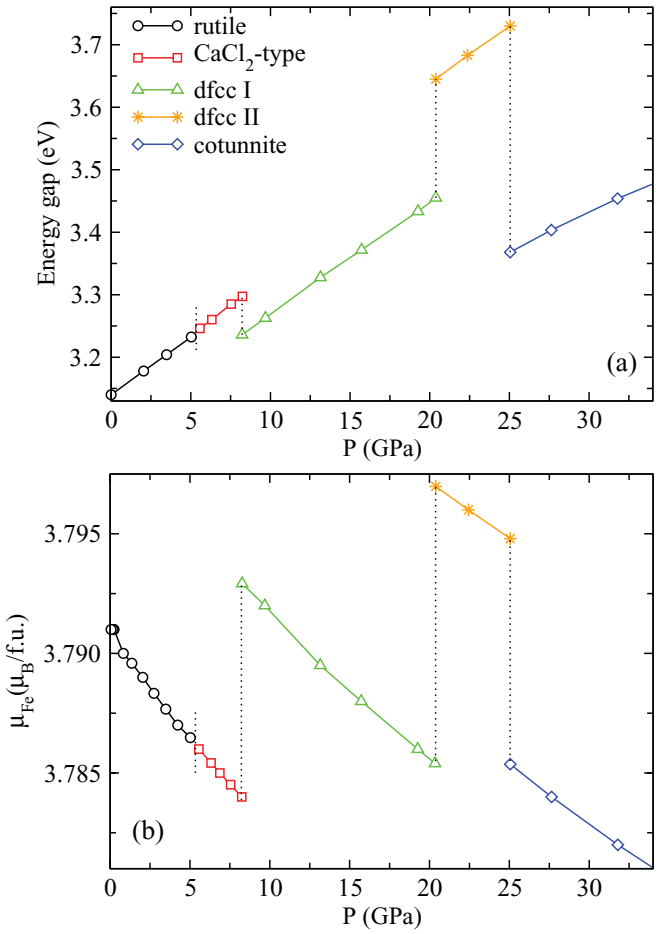

FIG. 11. (Color online) Calculated pressure dependences of (a) the energy gap and (b) the magnetic moment of Fe atom μ_{Fe} in μ_B per f.u. for all studied phases.

which results in the total change of only 0.63 eV over the entire range of 34 GPa. This is similar to ZnF_2, where a change in the band gap of ∼0.4 eV over the range of 35 GPa was observed.[27]

C. Magnetic exchange couplings

The Heisenberg theory of magnetism assumes that it is possible to describe magnetic interactions in a material by an effective Hamiltonian with localized spin moments as

$$H = -2\sum_{ij} J_{ij}\vec{S}_i\vec{S}_j, \quad (1)$$

where J_{ij} is the magnetic spin-coupling constant between two particular sites (i,j), and $\vec{S}_i$ is the spin on the site i. In a classical picture, this spin can be represented by a vector pointing in the direction of local magnetic moments on this site. The Heisenberg Hamiltonian is widely used to describe the magnetic properties of solids as well as molecules.

Our method of choice for the calculation of the exchange constants J_{ij} uses the energy differences approach. In this technique, the total energies of the equilibrium crystalline structure of several magnetic configurations are calculated, and these values are fitted to the Hamiltonian in Eq. (1). In the present case, four different spin states have to be taken into account to obtain three exchange constants J_1, J_2, and J_3, corresponding to the exchange coupling between the nearest, next-nearest, and third-nearest neighbor Fe^{2+} ions, respectively. In this procedure, three different cells have been considered: the first one is the conventional cell, the second is obtained by doubling the c axis, and the third one by doubling the surface of the basal plane of the conventional cell.

TABLE V. FeF_2 exchange couplings (in meV) for rutile and high-pressure phases: $CaCl_2$-type, dfcc I, dfcc II, and cotunnite.

	J_1	J_2	J_3
Rutile	0.033	−0.230	−0.020
$CaCl_2$-type	−0.039	−0.301	−0.019
dfcc I	−0.191	0.180	−0.025
dfcc II	−0.637	−0.047	0.963
Cotunnite	−0.084	−1.350	−0.178

The calculated exchange-coupling values for all phases are listed in Table V. We considered the spin of $S = 2$ for each Fe ion. In the case of the rutile phase, the exchange constants were determined from inelastic neutron scattering[94]: $J_1 = 0.003 \pm 0.004$ meV, $J_2 = -0.226 \pm 0.006$ meV, and $J_3 = -0.012 \pm 0.004$ meV. Our results are in good agreement with the experimental values. The spins are aligned ferromagnetically in the (001) plane (c plane) and antiferromagnetically between the planes, chiefly due to the dominant antiferromagnetic interaction J_2.

The $CaCl_2$-type phase also has a dominant antiferromagnetic interaction J_2, but with a larger value than that in the rutile phase. This is attributed to the decrease in the lattice parameter values when the pressure is applied.

The exchange couplings for dfcc I phase are very different from those of the previous two phases. There is a competition between the ferromagnetic interaction of Fe^{2+} nearest neighbors and the antiferromagnetic interactions of Fe^{2+} second neighbors. This is attributed to the change in the crystal structure and the fact that each Fe atom sees a different neighborhood. In this case, the interaction among nearest neighbors is mediated by fluorine atoms; because of that, J_1 is negative.

The crystal structure of the dfcc II phase has lattice parameters smaller than those in the dfcc I phase, and, therefore, larger values of the coupling constants. The magnetic configuration of the system changes from antiferromagnetic (dfcc I) to ferrimagnetic with three atoms coupled ferromagnetically (dfcc II). The cotunnite phase is again an antiferromagnetic crystal with a larger value J_2 due to higher pressure.

IV. SUMMARY AND CONCLUSIONS

We presented a systematic study of the structural, electronic, magnetic, and vibrational properties of FeF_2 compound at the rutile phase. The rutile phase is recognized to be the ground-state configuration for this compound. From this crystalline structure, using total-energy calculations of a large set of different crystalline phases, we follow the structural changes as a function of pressure by using the Gibbs free energy obtained from quasiharmonic approximation at 300 K.

The results show that the rutile phase is stable up to a pressure of 5.3 GPa and undergoes a second-order proper ferroelastic phase transition to the $CaCl_2$-type structure. It was observed that this transition is driven by the coupling between the Raman active B_{1g} mode and shear modulus C_s from the rutile phase. This transition was found in similar dioxide and fluoride rutile compounds, but it was not observed in previous high-pressure experiments for FeF_2. This could be due to limitations of the experimental setup. Thereafter, in agreement with the experiments, our results show that FeF_2 undergoes a phase transition to a crystalline distorted phase of $Pa\bar{3}$ group symmetry at about 8 GPa. The volume reduction of 7% at this transition pressure is in good agreement with the earlier experimental findings.

We also explored other possible high-pressure phases beyond the largest considered experimental pressure, and we found that a face-centered orthorhombic phase ($Fmmm$, another distorted fcc phase) was stable in the range of pressures from 20.38 to 25.05 GPa. As the pressure increases, the cotunnite-type structure becomes more stable than $Fmmm$-type structure, up to a pressure of 45 GPa. To corroborate or refute the experimental results for the phase transitions from the distorted fcc to a hexagonal phase, we studied 22 different hexagonal phases. We found that the energies of all those structures are not competitive against the high-pressure phases $CaCl_2$-type, dfcc I, dfcc II, and cotunnite reported in this work. Sensitive high-pressure experiments using a diamond anvil cell should be able to identify the structures reported here.

The coordination number for the first three phases for the Fe ions is 6, with the FeF_6 polyhedron more distorted in the $Pbca$ phase. For the $Fmmm$ phase, the coordination number is 8, and it becomes 9 for the $Pnma$ phase. We also observed that the magnetic moment values are rather insensitive to the Pressure change, while the exchange couplings reveal a large dependence on the crystalline structure and the interatomic distances.

After the lowest Gibbs free-energy structures were identified, a complete electronic and magnetic characterization was performed. In particular, we see the electronic gap changing from 3.14 eV for the rutile structure to 3.48 eV for the cotunnite structure. The magnetic moment changes slightly, and the system remains antiferromagnetic. The nearest-neighbor magnetic exchange couplings remain negative, while the coupling between the next-nearest neighbors changes. These changes should have an effect on the Néel temperature.

ACKNOWLEDGMENTS

This work was supported by CONACyT México under the Project No. J-152153-F (A.H.R.), PPPROALMEX-DAAD-Conacyt bi-national program (A.H.R.), Texas A&M University-CONACYT Collaborative Research Grant Program (A.H.R., I.V.R.), Texas A&M University (I.V.R.), UNAM México under a posdoctoral fellowship (S.L.-M.), FONDECYT grant 1100365, and Grant ICM P10-061-F by "Fondo de Innovacion para la Competitividad-MINECON" (J.M.-L.), MICINN of Spain under Grants No. MAT2010-21270-C04-03 and No. CSD2007-00045 (A.M.). The computer resources provided by RES (Red Española de Supercomputación) Spain (A.M.) and TACC (A.H.R., I.V.R.) are gratefully acknowledged. We thank Karie E. Badgley for her contribution to literature search.

*lsinhue@yahoo.com.mx

[1] M. Xu, Y. Gao, E. M. Moreno, M. Kunst, M. Muhler, Y. Wang, H. Idriss, and C. Wöll, Phys. Rev. Lett. **106**, 138302 (2011).
[2] H. A. Atwater and A. Polman, Nat. Mater. **9**, 205 (2010). .
[3] T. J. Yen, W. J. Padilla, N. Fang, D. C. Vier, D. R. Smith, J. B. Pendry, D. N. Basov, and X. Zhang, Science **303**, 1494 (2004).
[4] M. Li, X.-F. Yu, W.-Y. Yu, J. Zhou, X.-N. Peng, and Q.-Q. Wang, J. Phys. Chem. C **113**, 20271 (2009).
[5] I. Hernández, F. Rodríguez, and H. D. Hochheimer, Phys. Rev. Lett. **99**, 027403 (2007).
[6] L. G. Jacobsohn, K. B. Sprinkle, and S. A. Roberts, J. Nanomaterials **2011**, 523638 (2011).
[7] C. Zhang, C. Li, C. Peng, R. Chai, S. Huang, D. Yang, Z. Cheng, and J. Lin, Chem. Eur. J. **16**, 5672 (2010).
[8] V. B. Mikhailik and H. Kraus, Phys. Status Solidi B **247**, 1583 (2010).
[9] A. R. Oganov, G. D. Price, and S. Scandolo, Z. Kristallogr. **220**, 531 (2005).
[10] J. Zhao, A. V. Bragas, R. Merlin, and D. J. Lockwood, Phys. Rev. B **73**, 184434 (2006).
[11] D. J. Lockwood and M. G. Cottam, J. Appl. Phys. **64**, 5876 (1988).
[12] D. J. Lockwood, R. S. Katiyar, and V. C. Y. So, Phys. Rev. B **28**, 1983 (1983).
[13] M. Kiwi, J. Magn. Magn. Mater. **234**, 584 (2001).
[14] M. Marinelli, F. Mercuri, and D. P. Belanger, Phys. Rev. B **51**, 8897 (1995).
[15] G. Valerio, M. Catti, R. Dovesi, and R. Orlando, Phys. Rev. B **52**, 2422 (1995).
[16] L.-C. Ming and M. H. Manghnani, Geophys. Res. Lett. **5**, 491 (1978).
[17] L.-C. Ming, M. H. Manghnani, T. Matsui, and J. C. Jamieson, Phys. Earth Planet. Inter. **23**, 276 (1980).
[18] H. Wang, X. Liu, Y. Li, Y. Liu, and Y. Ma, Solid State Comm. **151**, 1475 (2011).
[19] C. Lee and X. Gonze, J. Phys.: Condens. Matter **7**, 3693 (1995).
[20] J. Haines, J. M. Léger, and O. Schulte, J. Phys.: Condens. Matter **8**, 1631 (1996).
[21] S. Ono, J. P. Brodholt, and G. D. Price, J. Phys.: Condens. Matter **20**, 045202 (2008).
[22] J. Haines, J. M. Léger, C. Chateau, and A. S. Pereira, Phys. Chem. Miner. **27**, 575 (2000).
[23] J. Haines and J. M. Léger, Phys. Rev. B **55**, 11144 (1997).
[24] S. S. Rosenblum, W. H. Weber, and B. L. Chamberland, Phys. Rev. B **56**, 529 (1997).
[25] B. R. Maddox, C. S. Yoo, D. Kasinathan, W. E. Pickett, and R. T. Scalettar, Phys. Rev. B **73**, 144111 (2006).
[26] J. Haines, J. M. Léger, and S. Hoyau, J. Phys. Chem. Solids **56**, 965 (1995).
[27] X. Wu, S. Qin, and Z. Wu, Phys. Rev. B **73**, 134103 (2006).

[28]J. D. Jorgensen, T. G. Worlton, and J. C. Jamieson, Phys. Rev. B **17**, 2212 (1978).
[29]J. Haines, J. M. Léger, F. Gorelli, D. D. Klug, J. S. Tse, and Z. Q. Li, Phys. Rev. B **64**, 134110 (2001).
[30]A. Perakis, D. Lampakis, Y. C. Boulmetis, and C. Raptis, Phys. Rev. B **72**, 144108 (2005).
[31]P. I. Sorantin and K. Schwarz, Inorg. Chem. **31**, 567 (1992).
[32]Y. Hazony and H. K. Perkins, J. Appl. Phys. **41**, 5130 (1970).
[33]Q.-J. Liu, Z.-T. Liu, L.-P. Feng, and H. Tian, Solid State Sci. **12**, 1748 (2010).
[34]K. R. Babu, C. B. Lingam, S. Auluck, S. P. Tewari, and G. Vaitheeswaran, J. Solid State Chem. **184**, 343 (2011).
[35]I. de P. R. Moreira, R. Dovesi, C. Roetti, V. R. Saunders, and R. Orlando, Phys. Rev. B **62**, 7816 (2000).
[36]P. Novák, J. Kunes, L. Chaput, and W. E. Pickett, Phys. Status Solidi B **243**, 563 (2006).
[37]A. Riss, P. Blaha, K. Schwarz, and J. Zemann, Z. Kristallogr. **218**, 585 (2003).
[38]V. Srivastava, M. Rajagopalan, and S. P. Sanyal, Eur. Phys. J. B **61**, 131 (2008).
[39]S. P. S. Porto, P. A. Fleury, and T. C. Damen, Phys. Rev. **154**, 522 (1967).
[40]C. Benoit and J. Giordano, J. Phys. C: Solid State Phys. **21**, 5209 (1988).
[41]M. Balkanski, P. Moch, and G. Parisot, J. Chem. Phys. **44**, 940 (1966).
[42]J. Giordano, E. Alaoui-Bichri, C. Benoit, R. Almairac, and A. M. Bon, J. Phys. Lett. **40**, 153 (1979).
[43]J. Giordano and C. Benoit, J. Phys. C: Solid State Phys. **21**, 2749 (1988).
[44]R. El Alaoui-Bichri, J. Giordano, R. Almairac, C. Benoit, and P. Nassiri, J. Phys. (France) **41**, 543 (1980).
[45]H. Ohta, C. Ramos, D. Lederman, and V. Jaccarino, J. Magn. Magn. Mater. **104–107**, 1741 (1992).
[46]M. Blanco, E. Francisco, and V. Luaa, Comput. Phys. Commun. **158**, 57 (2004).
[47]S. Baroni, S. Gironcoli, A. Dal Corso, and P. Giannozzi, Rev. Mod. Phys. **73**, 515 (2001).
[48]N. Nakagiri, M. H. Manghnani, Y. H. Kim, and L. C. Ming, in *High-Pressure Research in Mineral Physics*, edited by M. H. Manghnani and Y. Syono (Terra Scientific, Tokyo, Japan, 1987), pp. 281–287.
[49]J. Strempfer, U. Rütt, S. P. Bayrakci, T. Brückel, and W. Jauch, Phys. Rev. B **69**, 014417 (2004).
[50]P. E. Blöchl, Phys. Rev. B **50**, 17953 (1994).
[51]G. Kresse and D. Joubert, Phys. Rev. B **59**, 1758 (1999).
[52]G. Kresse and J. Hafner, Phys. Rev. B **47**, 558 (1993).
[53]G. Kresse and J. Hafner, Phys. Rev. B **49**, 14251 (1994).
[54]G. Kresse and J. Furthmüller, Comput. Mater. Sci. **6**, 15 (1996).
[55]G. Kresse and J. Furthmüller, Phys. Rev. B **54**, 11169 (1996).
[56]J. P. Perdew, K. Burke, and M. Ernzerhof, Phys. Rev. Lett. **77**, 3865 (1996).
[57]J. P. Perdew, K. Burke, and M. Ernzerhof, Phys. Rev. Lett. **78**, 1396 (1997).
[58]S. L. Dudarev, G. A. Botton, S. Y. Savrasov, C. J. Humphreys, and A. P. Sutton, Phys. Rev. B **57**, 1505 (1998).
[59]S. López, A. H. Romero, J. Mejía-López, J. Mazo-Zuluaga, and J. Restrepo, Phys. Rev. B **80**, 085107 (2009).
[60]H. Monkhorst and J. Pack, Phys. Rev. B **13**, 5188 (1976).
[61]P. E. Blöchl, O. Jepsen, and O. K. Andersen, Phys. Rev. B **49**, 16223 (1994).
[62]K. Parlinski, computer code PHONON. See http://wolf.ifj.edu.pl/phonon
[63]F. Birch, Phys. Rev. **71**, 809 (1947).
[64]W. Jauch, A. Palmer, and A. J. Schultz, Acta Crystallogr. B **49**, 984 (1993).
[65]J. W. Stout and S. A. Reed, J. Am. Chem. Soc. **76**, 5279 (1954).
[66]O. Gülseren and R. E. Cohen, Phys. Rev. B **65**, 064103 (2002).
[67]A. Y. Wu, R. J. Sladek, and R. S. Feigelson, Phys. Rev. B **26**, 1507 (1982).
[68]See Ref. 8 and references therein.
[69]A. Togo, F. Oba, and I. Tanaka, Phys. Rev. B **78**, 134106 (2008).
[70]H. Hellwig, A. F. Goncharov, E. Gregoryanz, H.-k. Mao, and R. J. Hemley, Phys. Rev. B **67**, 174110 (2003).
[71]J. Haines, J. M. Léger, C. Chateau, R. Bini, and L. Ulivi, Phys. Rev. B **58**, R2909 (1998).
[72]Y. Le Page and P. Saxe, Phys. Rev. B **65**, 104104 (2002).
[73]X. Wu, D. Vanderbilt, and D. R. Hamann, Phys. Rev. B **72**, 035105 (2005).
[74]D. S. Rimai, Phys. Rev. B **16**, 2200 (1977).
[75]D. Gerlich, S. Hart, and D. Whittal, Phys. Rev. B **29**, 2142 (1984).
[76]V. Kanchana, G. Vaitheeswaran, and M. Rajagopalan, Phys. B (Amsterdam) **328**, 283 (2003).
[77]J. M. Leger, J. Haines, A. Atouf, O. Schulte, and S. Hull, Phys. Rev. B **52**, 13247 (1995).
[78]V. Kanchana, G. Vaitheeswaran, and M. Rajagopalan, J. Alloys Comp. **359**, 66 (2003).
[79]A. Costales, M. A. Blanco, R. Pandey, and J. M. Recio, Phys. Rev. B **61**, 11359 (2000).
[80]L. Zhang, Y. Wang, T. Cui, Y. Ma, and G. Zou, Solid State Commun. **145**, 283 (2008).
[81]X. Wu and Z. Wu, Eur. Phys. J. B **50**, 521 (2006).
[82]S. S. Kabalkina, L. F. Vereshchagin, and L. M. Lityagina, Sov. Phys. Solid State **11**, 847 (1969).
[83]V. P. Prakapenka, G. Shen, L. S. Dubrovinsky, M. L. Rivers, and S. R. Sutton, J. Phys. Chem. Solids **65**, 1537 (2004).
[84]Y. Kuwayama, K. Hirose, N. Sata, and Y. Ohishi, Phys. Chem. Miner. **38**, 591 (2011).
[85]V. Meisalo and M. Kalliomäki, High Temp. High Press. **7**, 419 (1975).
[86]L.-G. Liu, W. A. Bassett, and J. Sharry, J. Geophys. Res. **10**, 2301 (1978).
[87]A. Mujica, A. Rubio, A. Munoz, and R. J. Needs, Rev. Mod. Phys. **75**, 863 (2003).
[88]D. Gerlich, S. Hart, and D. Whittal, Pure Appl. Chem. **79**, 1779 (2007).
[89]S. R. Shieh, A. Kubo, T. S. Duffy, V. B. Prakapenka, and G. Shen, Phys. Rev. B **73**, 014105 (2006).
[90]V. Swamy and B. C. Muddle, Phys. Rev. Lett. **98**, 035502 (2007).
[91]E. Shojaee, M. Abbasnejad, M. Saeedian, and M. R. Mohammadizadeh, Phys. Rev. B **83**, 174302 (2011).
[92]H. Dekura, T. Tsuchiya, and J. Tsuchiya, Phys. Rev. B **83**, 134114 (2011).
[93]L. S. Dubrovinsky, N. A. Dubrovinskaia, V. Swamy, J. Muscat, N. M. Harrison, R. Ahuja, B. Holm, and B. Johansson, Nature (London) **410**, 653 (2001).
[94]M. T. Hutchings, B. D. Rainford, and H. J. Guggenheim, J. Phys. C: Solid State Phys. **3**, 307 (1970).